



## Nanoparticle coagulation via a Navier–Stokes/nodal methodology: Evolution of the particle field

S.C. Garrick<sup>a,\*</sup>, K.E.J. Lehtinen<sup>b</sup>, M.R. Zachariah<sup>c</sup>

<sup>a</sup>*Department of Mechanical Engineering, 111 Church Street SE, University of Minnesota - Twin Cities, Minneapolis, MN 55455-0111, USA*

<sup>b</sup>*Department of Physics, University of Helsinki, Helsinki 00014, Finland*

<sup>c</sup>*Department of Mechanical Engineering, 111 Church Street SE, University of Minnesota - Twin Cities, Minneapolis, MN 55455-0111, USA*

Received 28 July 2003; received in revised form 19 April 2005; accepted 19 April 2005

### Abstract

Direct numerical simulation of a coagulating aerosol in a two-dimensional, incompressible, iso-thermal shear layer is performed. The evolution of the particle field is obtained by utilizing a nodal model to approximate the aerosol general dynamic equation (GDE). The GDE is written in discrete form as a population balance on each particle size and describes particle dynamics under the influence of various physical phenomena: convection, diffusion, and coagulation. The nodal approach is advantageous in that there are no a priori assumptions regarding the nature of the particle size distribution and therefore does not suffer from the severe constraints of other methodologies. This approach divides the particle size distribution into “bins,” for each of which a transport equation is obtained. A coagulation Damköhler number is defined to represent the ratio of the convective time scale to the coagulation time scale. Simulations are performed at a Reynolds number of 200 and coagulation Damköhler numbers of 1 and 10. The nanoparticle field is presented as a function of space, time and size. Results indicate that strong spatial variations in the particle concentrations develop in time and that these spatial gradients act to increase the geometric standard deviation of the particle size distribution. As the coagulation Damköhler number is increased, particle growth increases and particle size distributions wider than the self-preserving limit are predicted. The capture of the evolution of the particle field as a function of space, time and size suggests that the methodology is sufficiently general and robust to be useful in predicting the growth and dynamics in inhomogeneous, and possibly, turbulent flows.

© 2005 Elsevier Ltd. All rights reserved.

**Keywords:** Nanoparticles; Coagulation; Nodal methods; Direct numerical simulation; Navier–Stokes equations; Mixing layers

\* Corresponding author. Tel.: +1 612 624 5741; fax: +1 612 624 5230.

E-mail address: [garrick@me.umn.edu](mailto:garrick@me.umn.edu) (S.C. Garrick).

## 1. Introduction

Nanoscale particles play an integral role in a wide variety of physical/chemical phenomena and processes. These include but are not restricted to synthesis of nanostructured materials (nanoparticles and coatings). The market for nanostructured materials has dramatically increased in recent years with the growth of applications in industries such as microelectronics, cosmetics, chemical gas sensors, capacitors, and heat and mass transfer, amongst others. Nanostructured materials are expected to play an increasingly significant role in many major industries as we enter the new millennium (Wooldridge, 1998; Pratsinis, 1998; Dagani, 2000). There are several technologies which can be employed in the manufacture of nanoscale materials. Vapor-phase methodologies are favored because of chemical purity and cost considerations. The formation of very fine particles from vapor encompasses a large number of physical/chemical phenomena. When driven by gas-phase precursors one must address vapor-phase chemistry, particle nucleation, coagulation, coalescence, condensation, etc. (Pratsinis & Kim, 1989; Pratsinis, 1998; Wooldridge, 1998).

A key issue in the formation of nanoscale particles is the prevention of hard agglomerates and chemical control. For example, agglomeration can greatly diminish one of nanoparticles' chief advantages—their relatively high volume to surface-area ratio. Several strategies have been attempted to minimize agglomeration (Vemury & Pratsinis, 1995b; Kusters, Wijers, & Thoens, 1997; Vemury, Pratsinis, & Kibbey, 1997). Researchers have shown that agglomeration is dependent on the ratio of coalescence time to collision time, but the exact mechanism for this behavior is still a complex interaction of time–temperature and fluid mixing history (Zhu & Pratsinis, 1996; Lehtinen & Zachariah, 2001). The dynamics of particles in turbulent flows have received attention in the past several decades (Snyder & Lumley, 1971; Riley & Patterson, 1974; Elghobashi, 1991; Elghobashi & Truesdell, 1992). Squires and Eaton (1991) identified regions of flow fields which significantly influence particle transport and mixing, noting that the particle concentration in a turbulent flow field may become inhomogeneous. Eaton and Fessler (1994) focused on flows where the particle motion is determined only by its interaction with the fluid phase and found that the scale of preferential concentration of the particles is dependent on the particle time constant as well as where the Stokes number, based on the Kolmogorov scales, is near unity. Sundaram and Collins (1997) investigated the influence of particle parameters on collision frequencies and found that the magnitude of the minimum particle collision frequency is more strongly correlated to the turbulent motions at the integral scale. Reade and Collins (2000) considered the coagulation and growth of aerosol particles in an initially mono-disperse population of particles subjected to isotropic turbulence. The results revealed trends in the relative breadth of particle size distribution and its dependence on the Stokes number. However, the majority of these studies only considered larger, micron-sized particles. In a recent work, Wu and Menon (2001) studied the evolution of nanoscale particles in the near field of an engine exhaust plume using a moment method (Frenklach & Harris, 1987) in conjunction with a linear eddy method (LEM) (Kerstein, 1989, 1991, 1992; McMurtry, Menon, & Kerstein, 1993; Frankel, McMurtry, & Givi, 1995). However, the accuracy of the combined moment/LEM methodology was not established via comparison with results obtained experimentally or via direct numerical simulation (DNS). Nodal methods have been widely used in modeling particle formation and growth (Gelbard, Tambour, & Seinfeld, 1980; Seigneur et al., 1986; Zhang, Seigneur, Seinfeld, Jacobson, & Binkowski, 1999). The methodology consists of discretizing the particle field in size/volume space, and solving an evolution equation, or population balance, for each section. This methodology has been extended to two dimensions, describing the evolution of particle size and shape (Xiong & Pratsinis, 1993; Xiong, Akhtar, & Pratsinis, 1993; Jeong & Choi,

2003). Pyykönen and Jokiniemi (2000) employed nodal methods in conjunction with a Reynolds-averaged Navier–Stokes (RANS) solver to simulate aerosol formation and growth via nucleation, condensation and coagulation. This study neglected streamwise diffusion and the effects of turbulence on particle–particle interactions—products of concentration fluctuations—while the flows lacked recirculation. More robust methodologies which are capable of capturing transient flow effects and fluid turbulence are needed.

In this work DNS of nanoparticle coagulation in temporal mixing layers is performed. A nodal approach is used to represent the particle field. The flow field is obtained via solution of the incompressible Navier–Stokes equations. This approach facilitates the spatio-temporal evolution of the particle field and aids in elucidating the underlying structure of the particle–fluid interactions and vapor-phase particle growth due to Brownian coagulation (Seigneur et al., 1986; Zhang et al., 1999). Simulations are performed at two different initial volume fractions, and the particles range in diameter from 1 to 12 nm.

## 2. Governing equations

### 2.1. Fluid field

The flows under consideration are constant density shear flows containing nanoscale particles. The primary transport variables for the fluid field are the velocity vector  $u_i(\mathbf{x}, t)$ , and the fluid pressure  $p(\mathbf{x}, t)$ . These variables are governed by the conservation of mass and momentum equations

$$\frac{\partial u_j}{\partial x_j} = 0, \quad (1)$$

$$\frac{\partial u_i}{\partial t} + \frac{\partial u_i u_j}{\partial x_j} = -\frac{1}{\rho} \frac{\partial p}{\partial x_i} + \nu \frac{\partial^2 u_i}{\partial x_j \partial x_j}, \quad (2)$$

where  $\nu$  is the kinematic viscosity and  $\rho$  is the fluid density, taken to be unity (i.e.  $\rho = 1$ ). In addition, we consider the transport of a conserved scalar given by:

$$\frac{\partial \phi}{\partial t} + \frac{\partial \phi u_j}{\partial x_j} = \Gamma \frac{\partial^2 \phi}{\partial x_j \partial x_j}, \quad (3)$$

where  $\phi$  is the species concentration and  $\Gamma$  is the species diffusivity. In the flows under consideration, the species is inert and has no effect on the dynamics of the flow; it is used solely as a tracer species to characterize the mixing within the flow domain.

### 2.2. Particle field

The transport of the nanoscale particles dispersed throughout the fluid is governed by the aerosol general dynamic equation (GDE). The GDE describes particle dynamics under the influence of various physical and chemical phenomena—convection, diffusion, coagulation, surface growth, nucleation, and

other internal/external forces—and is given by (Friedlander, 2000)

$$\frac{\partial n}{\partial t} + \frac{\partial u_j n}{\partial x_j} + \frac{\partial I}{\partial v} = \frac{\partial}{\partial x_j} \left( D_n \frac{\partial n}{\partial x_j} \right) + \frac{1}{2} \int_0^v \beta(\tilde{v}, v - \tilde{v}) n(\tilde{v}) n(v - \tilde{v}) d\tilde{v} - \int_0^\infty \beta(v, \tilde{v}) n(v) n(\tilde{v}) d\tilde{v}, \quad (4)$$

where  $n(v)$  is the number of particles of volume  $v$ ,  $I$  is the nucleation rate,  $D_n$  is the diffusion coefficient and  $\beta$  is the collision frequency function for coagulation. From a practical standpoint such a system of equations cannot be solved explicitly except for very small particle sizes—less than 1000 molecular or “monomer” units. To overcome this and other issues, a nodal model is employed to describe the particle size distribution in time and space. The nodal method employed is the same as that of Lehtinen and Zachariah (2001) and Modem, Garrick, Zachariah, and Lehtinen (2002). Nodal methods are similar to sectional methods in that the particle field is discretized in volume space. The primary difference is that in sectional methods, the dependent variables (particle concentrations) typically represent a range of sizes, whereas in nodal methods, the dependent variables correspond to particles of a particular size (Gelbard & Seinfeld, 1980). The advantage of the nodal approach, in comparison to the sectional, is the great simplification of the integrals appearing in the coagulation/growth terms; these are reduced to sums in the nodal approach but require costly numerical integration in the sectional approach. Nodal/sectional methods are advantageous in that there are no a priori assumptions regarding the nature of the particle size distribution and they do not suffer from the severe constraints of other methodologies such as moment methods (Gelbard et al., 1980; Seigneur et al., 1986; Zachariah & Semerjian, 1989; Xiong & Pratsinis, 1993; McGraw, 1997; Wright, McGraw, & Rosner, 2001; Terry, McGraw, & Rangel, 2001; Settumba & Garrick, 2003). In this work we consider particles between 1 and 12.7 nm in diameter, those typically consisting of thousands of molecules. The evolution of these particles is captured by solving a set of  $N_s$  transport equations, one for the concentration of particles in each bin,  $Q_k$ ,  $k = 1, 2, \dots, N_s$ . The number concentration  $Q_k(\mathbf{x}, t)$  changes due to the effects of large-scale and small-scale transport (convection, diffusion, etc.) as well as particle formation and growth processes. The number of particles in bin  $k$  at location  $\bar{x}$  and time  $t$  is given by

$$\frac{\partial Q_k}{\partial t} + \frac{\partial Q_k u_j}{\partial x_j} = \mathcal{D}_k \frac{\partial^2 Q_k}{\partial x_j \partial x_j} + \omega_k, \quad (5)$$

where  $D_k$  is the particle diffusivity given by

$$\mathcal{D}_k = k_b T \frac{C_c}{3\pi\mu d_p}, \quad (6)$$

$k_b$  is the Boltzmann constant,  $T$  is the fluid temperature,  $C_c$  is the Cunningham correction factor (Fuchs, 1964; Reist, 1993),  $\mu = \rho\nu$  is the viscosity,  $d_p$  is the particle diameter and  $\omega_k$  is the source term given by

$$\omega_k = \frac{1}{2} \sum_{i=1}^{N_s} \sum_{j=1}^{N_s} \beta_{ij} \chi_{ijk} Q_i Q_j - \sum_{i=1}^{N_s} \beta_{ik} Q_i Q_k. \quad (7)$$

The source term,  $\omega_k$ , represents particle–particle interactions leading to Brownian coagulation: production of particles in bin  $k$  due to collisions of smaller particles; the loss and gain of particles in bin  $k$  by collision

with a particle which either moves the resulting particle out of, or into, bin  $k$ ; and the loss of particles in bin  $k$  as they collide with each other and form larger particles. All effects except for nanoparticle coagulation are neglected. It should be noted that repeated indices in Eq. (7) do not imply summation but instead infer interactions between particles. The collision frequency function  $\beta_{ij}$  in the free-molecular regime is given by

$$\beta_{ij} = \left(\frac{3}{4\pi}\right)^{1/6} \left(\frac{6k_b T}{\rho_p}\right)^{1/2} \left(\frac{1}{v_i} + \frac{1}{v_j}\right)^{1/2} \left(v_i^{1/3} + v_j^{1/3}\right)^2, \quad (8)$$

where  $v_i$  is the volume of a particle in bin  $i$ ,  $\rho_p$  is the particle density and  $\chi_{ijk}$  is given by

$$\chi_{ijk} = \begin{cases} \frac{v_{k+1} - (v_i + v_j)}{v_{k+1} - v_k} & \text{if } v_k \leq v_i + v_j < v_{k+1}, \\ \frac{(v_i + v_j) - v_{k-1}}{v_k - v_{k-1}} & \text{if } v_{k-1} \leq v_i + v_j < v_k, \\ 0 & \text{otherwise.} \end{cases} \quad (9)$$

The particle field is discretized in size space such that the volume of particles in two successive bins is doubled, i.e.  $v_k = 2 \times v_{k-1}$ . This discretization scheme allows us to span a volume range of  $V = v_1$  to  $2^{N_s-1} \times v_1$ . Because of the logarithmic spacing of particle sizes, a collision of two particles typically results in a size that lies between bins. The operator  $\chi_{ijk}$  “splits” such particles into neighboring bins in such a way that the total particle mass is preserved. The collision frequency function’s form comes from the kinetic theory of gases (the particle diameters are smaller than the mean free path of the carrier gas) under the assumption that inter-particle forces are insignificant, e.g. electrostatic, van der Waals (Hamaker, 1937; Lifshitz, 1956; Langbein, 1974; Kerminen, 1994). Our studies are confined to particles in the free molecule regime ( $Kn > 1$ ). This implies that, in air (at 300 K), mean free paths over 65 nm are expected and growth of aerosols for sizes below this value can be based on one form of the collision frequency function  $\beta_{ij}$ . An additional simplification in working with small particle sizes is that the Stokes number is sufficiently small so as to imply that particle velocity slip can be neglected and we can treat the whole problem as a single phase flow, i.e. particle inertial effects can be ignored (Fuchs, 1964).

Implicit in this formulation of  $\beta_{ij}$  is the assumption that coalescence processes are effectively instantaneous and all particles are spherical. However, we do know that agglomeration will take place once the collision rate between particles is faster than the coalescence rate (Lehtinen & Zachariah, 2001). For example, this regime is typically reached under combustion conditions where metal oxides grow as primary particles greater than about 30 nm for most materials (e.g. silica, titania, etc.). For our simulations, particles are significantly below this threshold value and the assumption of instantaneous coalescence is valid. It has been shown that for small aggregate growth the use of the spherical assumption in the formulation of the collision frequency function under-predicts the collision rate by a factor of two or three (Vemury & Pratsinis, 1995a). Methods to correct for non-spherical aggregate formation have been developed and provide a convenient and simple modification to the collision frequency function  $\beta_{ij}$  and can be included in subsequent work (Koch & Friedlander, 1990; Matsoukas & Friedlander, 1991; Friedlander & Wu, 1994; Lee, Oh, & Choi, 2001; Lehtinen & Zachariah, 2002).

The chief disadvantage of the nodal approach is the computational expense which arises from the need to solve an additional transport equation for the concentration of particles in each bin. This expense is compounded by the size-dependent diffusion coefficient,  $\mathcal{D}_k$ . Moment-based methods offer solution

methodologies which are more computationally affordable but they are not as general as the nodal approach (McGraw, 1997; Terry et al., 2001; Wright et al., 2001, 2002). This generality, admittedly, comes with longer compute-times, as will be shown later.

### 2.3. Non-dimensionalization

The governing equations for the fluid and particle fields share several flow variables and molecular properties. To simplify the treatment and analysis of the interactions between the fluid and particle fields, the governing equations are non-dimensionalized. This is accomplished using the following relations and is similar to that performed by Settumba and Garrick (2003):

$$x_i^* = \frac{x_i}{L}, \quad t^* = \frac{t}{L/U_0}, \quad u_k^* = \frac{u_k}{U_0}, \quad p^* = \frac{p}{\rho U_0^2}, \quad \phi^* = \frac{\phi}{\phi_0}, \quad Q_k^* = \frac{Q_k}{Q_0}, \quad \beta_{ij}^* = \frac{\beta_{ij}}{\beta_0}. \quad (10)$$

The characteristic length scale is  $L$ , and the characteristic velocity  $U_0$ . The conserved scalar is non-dimensionalized by a reference species concentration  $\phi_0$ . The particle number concentration  $Q_k$  is non-dimensionalized by a reference concentration  $Q_0$ , and the collision frequency function is non-dimensionalized by a characteristic collision frequency  $\beta_0$ . Substituting the relations given in Eq. (10) into Eqs. (1)–(3) yield the familiar mass, momentum, and species conservation equations

$$\frac{\partial u_j^*}{\partial x_j^*} = 0, \quad (11)$$

$$\frac{\partial u_i^*}{\partial t^*} + \frac{\partial u_i^* u_j^*}{\partial x_j^*} = -\frac{\partial p^*}{\partial x_i^*} + \frac{1}{Re_L} \frac{\partial^2 u_i^*}{\partial x_j^* \partial x_j^*}, \quad (12)$$

$$\frac{\partial \phi^*}{\partial t^*} + \frac{\partial \phi^* u_j^*}{\partial x_j^*} = \frac{1}{Re_L Sc_\phi} \frac{\partial^2 \phi^*}{\partial x_j^* \partial x_j^*}. \quad (13)$$

The Reynolds number,  $Re_L = U_0 L / \nu$ , is the familiar ratio of inertial to viscous forces, and the Schmidt number,  $Sc_\phi = \nu / \Gamma$ , represents the ratio of momentum to species mass diffusivity. Similarly, the transport equation for the particulate phase is given by

$$\frac{\partial Q_k^*}{\partial t^*} + \frac{\partial Q_k^* u_j^*}{\partial x_j^*} = \frac{1}{Re_L Sc_k} \frac{\partial^2 Q_k^*}{\partial x_j^* \partial x_j^*} + \omega_k^*, \quad (14)$$

where  $Sc_k = \nu / \mathcal{D}_k$  is the Schmidt number of particles in bin  $k$ , and the source term is given by

$$\omega_k^* = \frac{1}{2} Da \sum_{i=1}^{N_s} \sum_{j=1}^{N_s} \beta_{ij}^* \chi_{ijk} Q_i^* Q_j^* - Da \sum_{i=1}^{N_s} \beta_{ik}^* Q_i^* Q_k^*. \quad (15)$$

The term  $Da$  is analogous to the convective Damköhler number in the reacting flows literature and represents the ratio of the particle collision, or coagulation, time scales to the convective time scales and is given by

$$Da = \frac{L}{U_0} \frac{\Phi}{\nu_1} \beta_0, \quad (16)$$

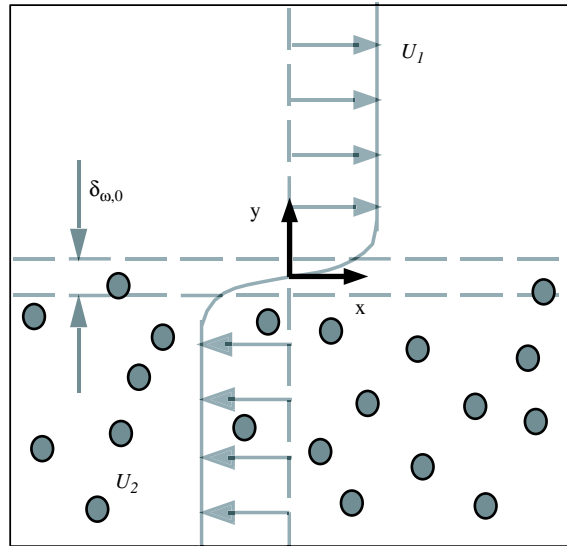


Fig. 1. Temporal mixing layer flow configuration.

where  $\Phi$  is the volume fraction, defined as the ratio of the volume of the particles to the volume of the fluid, and  $v_1$  is the volume of a particle in bin 1. In the flows under consideration, the characteristic length and velocity scales, as well as volume fraction, are the primary means of controlling the rate of coagulation. Though the collision frequency,  $\beta_{ij}^*$ , is a function of the fluid temperature and density, we consider only incompressible and iso-thermal flows. Therefore the rate of collisions between particles in bins  $i$  and  $j$  is a constant. Damköhler numbers of zero and infinity represent the limiting flow conditions; zero indicates that particles do not collide/coagulate, while infinity implies that collisions occur instantaneously and all particles are instantaneously converted to the largest particle represented by the nodal method. This definition of a coagulation Damköhler number is similar to that defined by Kennedy (1998) in modeling nucleation as a polymerization process.

### 3. Results

#### 3.1. Flow configuration

The flows under consideration are two-dimensional, incompressible mixing layers. A temporal mixing layer is formed when two parallel streams which travel in the opposite direction meet (Riley & Metcalfe, 1980; Sandham & Reynolds, 1991; Moser & Rogers, 1993). The streams mix and entrain fluid through large-scale coherent structures (Brown & Roshko, 1974; Roshko, 1976; Cain, Reynolds, & Ferziger, 1981; Bernal & Roshko, 1986; Miller, Madnia, & Givi, 1994). The space coordinates are  $\mathbf{x} = (x, y)$ , where  $x$  is the streamwise direction, and  $y$  is the cross-stream direction, as shown in Fig. 1. The velocity is initialized with a hyperbolic tangent profile in the cross-stream direction. The formation of large-scale structures is expedited through the addition of eigenfunction-based perturbations to the velocity field (Metcalfe, Orszag, Brachet, Menon, & Riley, 1987; Lee & Chen, 1984). The fluid in this study is air at 300 K. All

Table 1  
Particle sizes and Schmidt numbers

| Section, $k$ | Diameter, $d_p$ (nm) | Particle Schmidt number, $Sc_k$ |
|--------------|----------------------|---------------------------------|
| 1            | 1.00                 | 3.23                            |
| 2            | 1.26                 | 5.13                            |
| 3            | 1.59                 | 8.13                            |
| 4            | 2.00                 | 12.89                           |
| 5            | 2.52                 | 20.43                           |
| 6            | 3.17                 | 32.37                           |
| 7            | 4.00                 | 51.26                           |
| 8            | 5.04                 | 81.13                           |
| 9            | 6.35                 | 128.29                          |
| 10           | 8.00                 | 202.69                          |
| 11           | 10.08                | 319.83                          |
| 12           | 12.70                | 503.89                          |

flows have a Reynolds number based on the vorticity thickness,  $L = \delta_\omega$ , and the velocity difference,  $U_0 = (U_1 - U_2)/2$ , of  $Re_L = U_0 L / \nu = 200$ . Initially, the lower stream (stream 2) is seeded with particles of diameter 1 nm while the upper stream (stream 1) is devoid of particles. The reference concentration is taken to be the initial number of 1 nm particles in the particle-laden stream, i.e.  $Q_0 = Q_1(\mathbf{x}, 0)$ , and the characteristic collision frequency is taken to be the rate at which these particles collide, i.e.  $\beta_0 = \beta_{11}$ . A total of 12 bins are solved for, i.e.  $N_s = 12$ . The Schmidt numbers of the nanoparticles,  $Sc_k$ , span two orders of magnitude and are tabulated in Table 1. Two different Damköhler number flows are simulated,  $Da = 1$  and 10. These correspond to volume fractions of  $10^{-9}$  and  $10^{-8}$ , respectively. In addition to the nanoparticles, the lower stream contains a passive scalar  $\phi$ . The value of the molecular Schmidt number for the conserved scalar,  $\phi$ , is chosen to be identical to that of the 1 nm particles, i.e.  $Sc_\phi = Sc_k, k = 1$ . With this value, the dynamics observed in the conserved scalar are the same as those of the particles contained in the first bin without the effect of coagulation.

### 3.2. Numerical specifications

The governing transport equations are solved using a hybrid MacCormack-based compact difference scheme (MacCormack, 1969; Carpenter, 1990). The numerical scheme used is based on the one-parameter family of dissipative two–four schemes developed by Carpenter (1990). The accuracy of the scheme is second order in time and fourth order in space. The exact details of the numerical schemes employed in this study are not given here but a catalog of these schemes and others is readily available (Carpenter, 1990; Kennedy & Carpenter, 1994). Computations are performed on a domain of  $2\pi \times 2\pi$  in the streamwise,  $x$ , and cross-stream,  $y$ , directions, respectively. As the flow evolves in time, particles are convected and diffuse throughout the domain. Periodic boundary conditions are used in the streamwise  $x$ -direction, while zero-derivative conditions are used in the cross-stream  $y$ -direction. The periodic condition implies that fluid and particles, exiting through the left or right boundary are re-introduced through the right or left boundary, respectively. The computational grid is evenly spaced,  $\Delta_x = \Delta_y$ , and is comprised of  $1500 \times 1500$  grid points. A large number of grid points is required for the relatively low Reynolds number flow because of the high Schmidt numbers of the particle field. The grid resolution was chosen such that

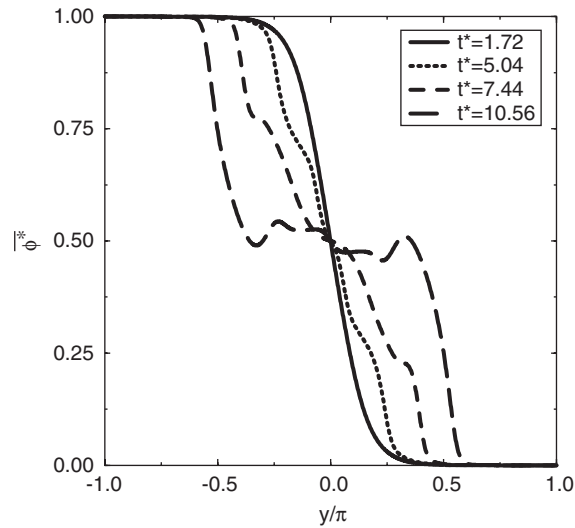


Fig. 2. Cross-stream variation of conserved scalar ( $\phi$ ).

the solution of the particle field is grid independent. Each simulation required roughly 1350 CPU hours on a SGI 3800 computer.

### 3.3. Scalar field

The simulations provide the entire particle field as a function of space, time and size. To facilitate qualitative and quantitative assessments of particle field dynamics both instantaneous and averaged data are presented. The averaging is performed in the homogeneous  $x$ -direction and contains 1500 samples. The eddies macroscopically mix fluid from the two streams as they “roll up” and pair. As time increases, the scalar concentration increases in stream 1, decreases in stream 2, and remains constant at the interface of the two streams. A quantitative view of the scalar evolution is presented in Fig. 2. As fluid containing the inert species moves from streams 1 to 2, the same amount of fluid (devoid of the inert conserved scalar) moves from streams 2 to 1. This is due to the nature of the initial perturbations in the velocity field, which cause the mixing layer to develop in a symmetric manner. This symmetry is readily observed in the cross-stream concentration profiles. It should be noted that the scalar  $\phi$  has the same diffusivity as the 1 nm diameter particles and thus represents the dynamics that particles in bin 1 would realize without the effects of coagulation. The conserved scalar contours portray the effects of convection and diffusion only; the effects of coagulation are neglected. Under these conditions, the mass of particles in bins 2–12 is zero, as they are not present initially and the mechanism facilitating particle growth is removed.

### 3.4. Particle field

Cross-stream profiles of the 1 nm diameter particle concentration are presented in Fig. 3. The ordinate spans across the height of the mixing layer—the region  $y < 0$  being the particle-laden stream and the region  $y > 0$  being the initially particle-free stream—with the abscissa containing the normalized particle

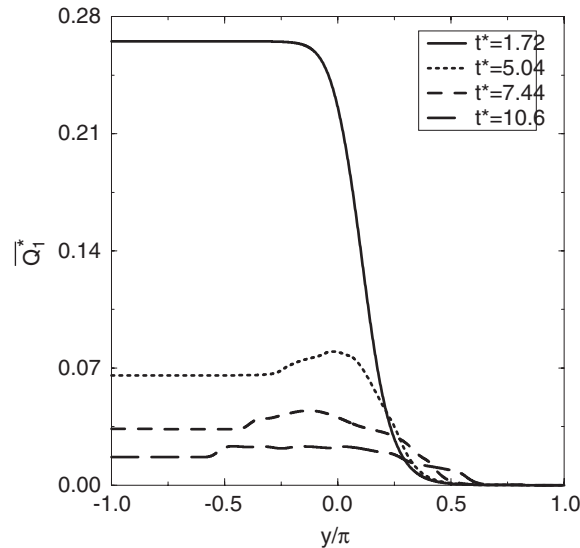


Fig. 3. Cross-stream variation of 1 nm diameter particle concentration  $\overline{Q}_1^*$  ( $Da = 1$ ).

concentration. All concentrations are normalized by the number of particles of size 1 nm in diameter in the initially particle-laden stream at time  $t^* = 0$ ,  $Q_{10}$ . Therefore at time  $t^* = 0$ ,  $\overline{Q}_1^*$  is zero in the particle-free stream and unity in particle-laden stream. The concentration gradient across the mixing layer acts to transport particles from the particle-laden stream into the particle-free stream. The figure reveals that at time  $t^* = 1.72$  the concentration of particles in the particle-laden stream decreases to  $\overline{Q}_1^* = 0.26$ . That is, 26% of the initial number of particles remain. By time  $t^* = 10.6$  the concentration of 1 nm particles is less than 2% of the initial concentration. This decrease is the result of collisions due to Brownian collisions. As the particles collide they grow in size, moving from lower-numbered to higher-numbered bins. Additionally, because of the absence of effects such as particle break-up, evaporation or surface chemistry, particles do not decrease in size and cannot move from higher- to lower-numbered bins. The rate of decrease is proportional to the square of the particle number concentration (Eq. (15)). Fig. 3 also reveals the non-linear nature of the coagulation source term. For example, the profiles show that by time  $t^* = 5.04$  the number of 1 nm diameter particles in the particle-laden stream is less than in the core of the eddy, the region  $-0.25 \leq y/\pi \leq 0.25$ . Mixing of the particle-free and particle-laden streams occurs in the eddy core. This mixing acts to reduce the particle number concentration, which reduces the growth rate. Additionally, the profiles also reveal the dispersion and transport of particles across the mixing layer.

The temporal evolution of the 1.26 nm diameter particles is shown in Fig. 4. The cross-stream profiles are similar to that observed in  $\overline{Q}_1^*$ . Initially zero, the concentration  $\overline{Q}_2^*$  in the particle-laden stream decreases between times  $t^* = 1.72$  and 10.56. This means that prior to  $t^* = 1.72$  the number of particles has increased from  $\overline{Q}_2^* = 0$  to a maximum value. Unlike the smallest 1 nm diameter particles, the source term for the 1.26 nm particles  $\omega_2^Q$ , can be both positive and negative. Neglecting 2 nm and larger particles, the source term for the 1.26 nm diameter particle concentration is given by

$$\omega_2^Q = \frac{1}{2}\beta_{11}Q_1Q_1 + \beta_{12}\chi_{122}Q_1Q_2 - (\beta_{12}Q_1Q_2 + \beta_{22}Q_2Q_2 + \beta_{32}Q_3Q_2). \quad (17)$$

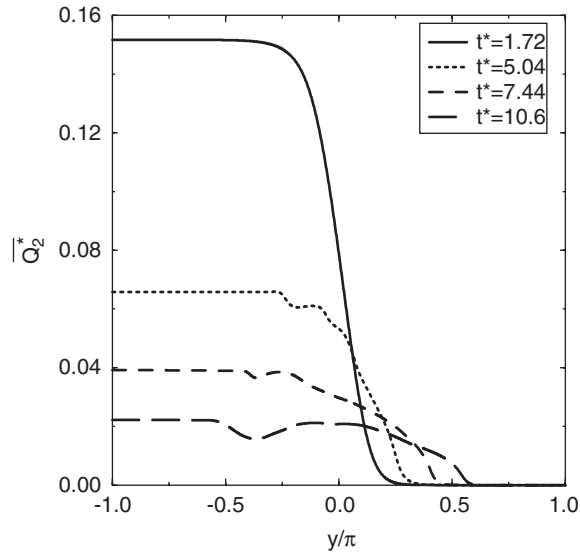


Fig. 4. Cross-stream variation of 1.26 nm diameter particle concentration  $\overline{Q_2^*}$  ( $Da = 1$ ).

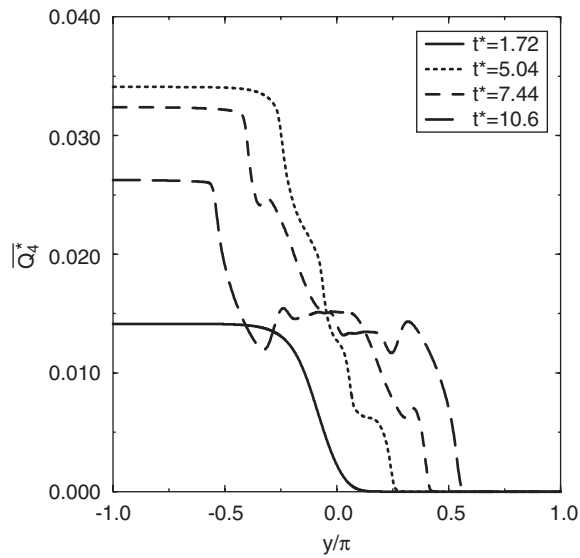


Fig. 5. Cross-stream variation of 2 nm diameter particle concentration  $\overline{Q_4^*}$  ( $Da = 1$ ).

The monotonic (in time) decrease of  $\overline{Q_2^*}$  in the particle-laden stream indicates that the first two terms on the RHS of Eq. (17) are zero and the only contribution is the removal of particles from bin 2. The migration of particles into the initially particle-free stream is more easily observed in Fig. 4.

Cross-stream profiles of the 2 nm diameter particles are shown in Fig. 5. The temporal evolution of these particles is somewhat different than that observed in the smaller 1 and 1.26 nm particles. The figure

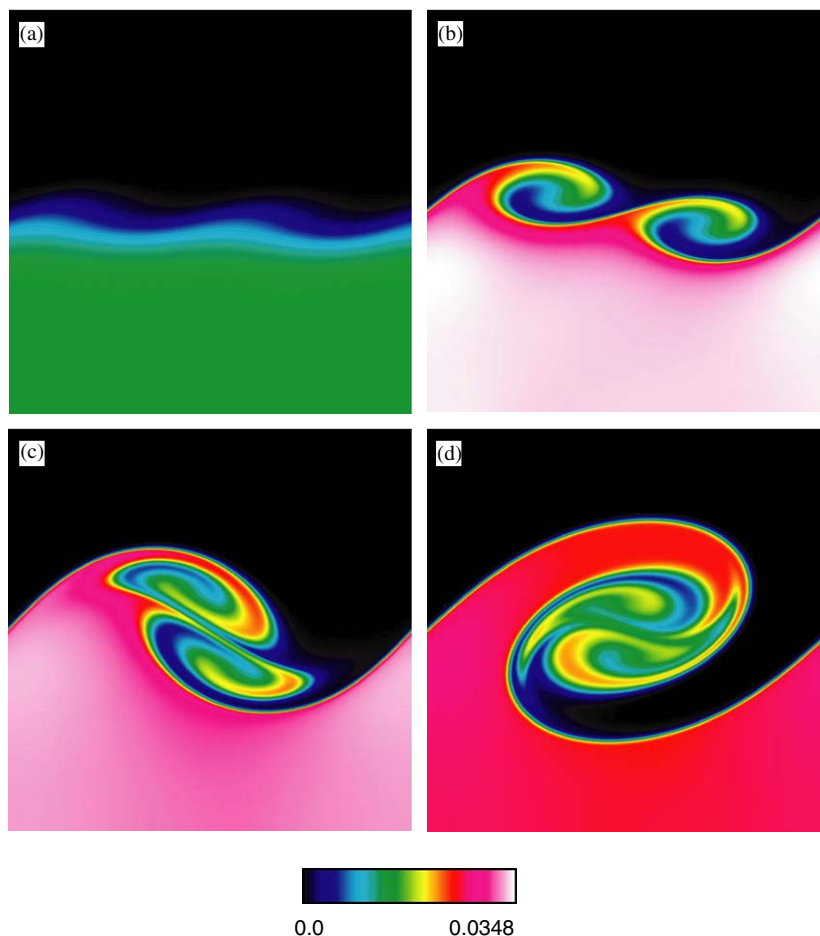


Fig. 6. Instantaneous 2 nm diameter particle concentration contours ( $Da = 1$ ): (a)  $t^* = 1.72$ ; (b)  $t^* = 5.04$ ; (c)  $t^* = 7.44$ ; (d)  $t^* = 10.6$ .

shows that between  $t^* = 1.72$  and  $5.04$  the concentration of 2 nm particles increases, while after  $t = 5.04$  the number of particles decreases. This time period captures the increase, peak, and decrease of particles in bin 4. Interestingly, the number of 2 nm particles near the interface of the two streams increases to a value of  $\overline{Q}_4^* = 0.015$  and remains there for the duration of the simulation, i.e.  $\partial \overline{Q}_3^* / \partial t|_{y=0} = 0$ . The migration of particles across the mixing layer from the particle-laden to the particle-free stream is also observed in Fig. 5. At time  $t^* = 10.6$ , the peak concentration in the initially particle-free stream is roughly 50% of that in the initially particle-laden stream. Instantaneous contours of the 2 nm particle concentration are shown in Fig. 6. The spatio-temporal evolution of the 2 nm particle field is elucidated in this sequence of images. The images show the formation, growth, and pairing of two eddies. During this process, the particle-laden stream engulfs a region of fluid from the originally particle-free stream. This region goes on to become the eddy core. Figs. 6(b)–(d) show that though there is some variation across the eddy core, the concentration of 2 nm particles within the eddy core remains roughly constant between time  $t^* = 5.04$  and  $10.6$ .

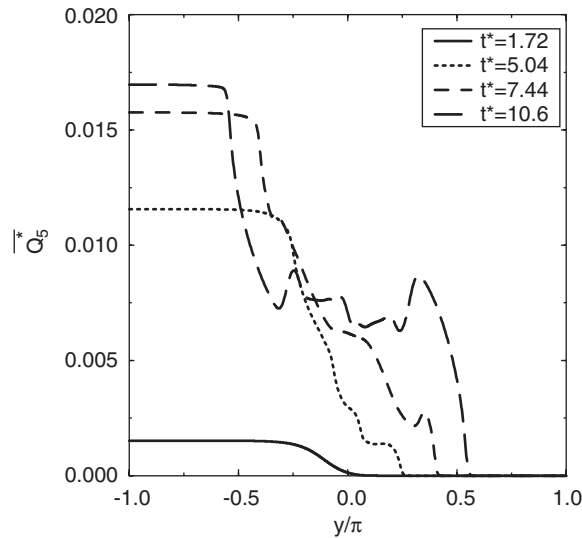


Fig. 7. Cross-stream variation of 2.52 nm diameter particle concentration  $\overline{Q}_5^*$  ( $Da = 1$ ).

Cross stream profiles of the 2.52 nm particle concentration are shown in Fig. 7. The figure shows that while the concentration  $\overline{Q}_5^*$  is increasing, the particle concentration rate of change is decreasing with time in the particle-laden stream. The profiles also capture the mixing of particle-laden and particle-free fluid observed in Fig. 6; between time  $t^* = 7.44$  and 10.6,  $\overline{Q}_5^*$  decreases in the region  $-\pi/2 < y < -\pi/4$ . During the same time interval the conserved scalar,  $\phi$ , also undergoes the largest decrease in concentration, suggesting that the change in  $\overline{Q}_5^*$  is not due to particle growth only. The drop in concentration is due to the influx of particle-free fluid which acts to dilute the particle field. The dilution manifests itself as a decrease in the concentration  $\overline{Q}_5^*$ . The concentration decrease propagates through the entire particle field as the growth rate is reduced in this region. Cross-stream 3.17 nm diameter particle concentration profiles are shown in Fig. 8. The profiles show that the concentration  $\overline{Q}_6^*$  generally increases with time. The effects of dilution are also seen in the concentration profiles. The largest number of particles are found in the particle-laden stream while the number of particles in the eddy core is relatively low. The evolution of the 4 nm and larger particles is very similar to that of the 3.17 nm particles and is omitted for brevity. The profiles are of the same general shape; differences are found only in the magnitude of the particle concentration and these profiles are also omitted for brevity.

The structure of the particle field may be observed by considering the spatial distribution of the particles by size. Instantaneous contours of the 1, 2, 4 and 8 nm diameter particles in the  $Da = 10$  flow at time  $t^* = 10.6$  are shown in Fig. 9. The particle concentration images reveal a degree of spatial segregation of different size particles. The highest concentrations of 1 nm particles are along the interface of the two streams and in the pocket of initially particle-free fluid being engulfed by the particle-laden stream. Fig. 9(a) shows that by time  $t^* = 10.6$  the particle-laden stream is nearly devoid of 1 nm particles. Fig. 9(b) shows that the number of 2 nm diameter particles is highest near the eddy core. The concentration in the core is between 50% and 100% greater in this region compared to the particle-laden stream. Fig. 9(c) shows that the concentration of 4 nm particles is more uniformly distributed throughout the particle-containing fluid. The concentration of 8 nm diameter particles is shown in Fig. 9(d). This image shows

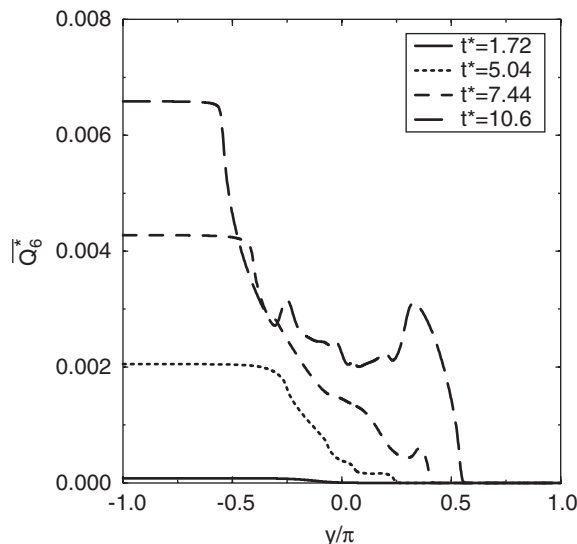


Fig. 8. Cross-stream variation of 3.17 nm diameter particle concentration  $\overline{Q_6^*}$  ( $Da = 1$ ).

that the largest number of 8 nm particles are found in the particle-laden stream, while concentrations in the eddy core range between zero and 50% of the maximum value. The separation by size reflects differences in growth rate throughout the flow domain. Particles coagulate faster in the particle-laden stream, as the concentration is highest. The effects of large-scale convection, which brings particle-free fluid into contact with particle-laden fluid, and diffusion, which mixes the two, are to dilute the particle concentration to varying degrees and create strong spatial variations. Such “maps” illustrating the particle field as a function of space, time, and size can illustrate particle collisions by size. For example, Fig. 9 suggests that collisions between 1 and 8 nm particles will primarily occur in a thin region near the interface of the particle-laden and particle-free streams, while collisions between 4 and 8 nm are more distributed. The former is analogous to diffusion flames in the turbulent reacting flow literature, while the latter is analogous to premixed flames (Williams, 1985). The simulation of premixed and non-premixed combustion requires different modeling strategies (Williams, 1989). Models and closures employed in the simulation of such flows may be useful in performing large eddy simulation or RANS of nanoparticle-containing flows (Libby & Williams, 1994; Wu & Menon, 2001).

### 3.5. Effect of the coagulation Damköhler number

The coagulation Damköhler number,  $Da$ , is varied by increasing the initial volume fraction  $\Phi$ . The effect of the coagulation Damköhler number is quantified by considering the evolution of the average particle size and the geometric standard deviation (GSD) of the particle size distribution. The evolution of the average particle size reflects the growth rate while the GSD reflects the width of the particle size distribution. The mean particle diameter is given by  $d_m = (6/\pi v_m)^{1/3}$ , where the mean volume is computed

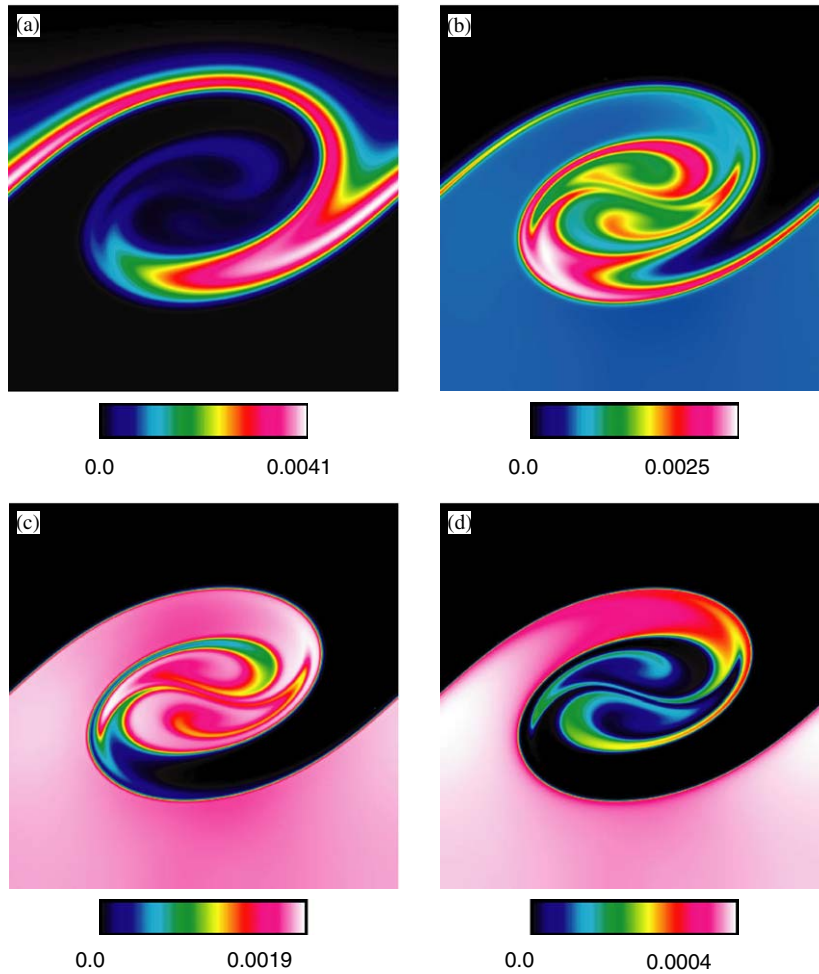


Fig. 9. Instantaneous particle concentration contours at  $t^* = 10.6$  ( $Da = 10$ ): (a)  $d_p = 1$  nm; (b)  $d_p = 2$  nm; (c)  $d_p = 4$  nm and (d)  $d_p = 8$  nm.

from the bin concentrations via

$$v_m = \frac{\sum Q_i v_i}{\sum Q_i}. \quad (18)$$

Cross-stream profiles of the mean particle diameter for the  $Da = 1$  flow are shown in Fig. 10(a). The profiles show that the particles in the initially particle-laden stream increase from an initial mean size of 1–2 nm by time  $t^* = 10.6$ . At the same time, the largest mean diameter in the eddy core is roughly 1.6 nm. The profiles also reflect the local effects of dilution observed in Fig. 7, as the mean particle diameter decreases near  $y/\pi = -0.38$  between  $t^* = 7.44$  and 10.6. Cross-stream profiles for the  $Da = 10$  flow are shown in Fig. 10(b). The trend is the same as observed in the  $Da = 1$  flow. The primary difference is the magnitude of the mean diameter. At time  $t^* = 1.72$  the mean diameter in the particle-laden stream

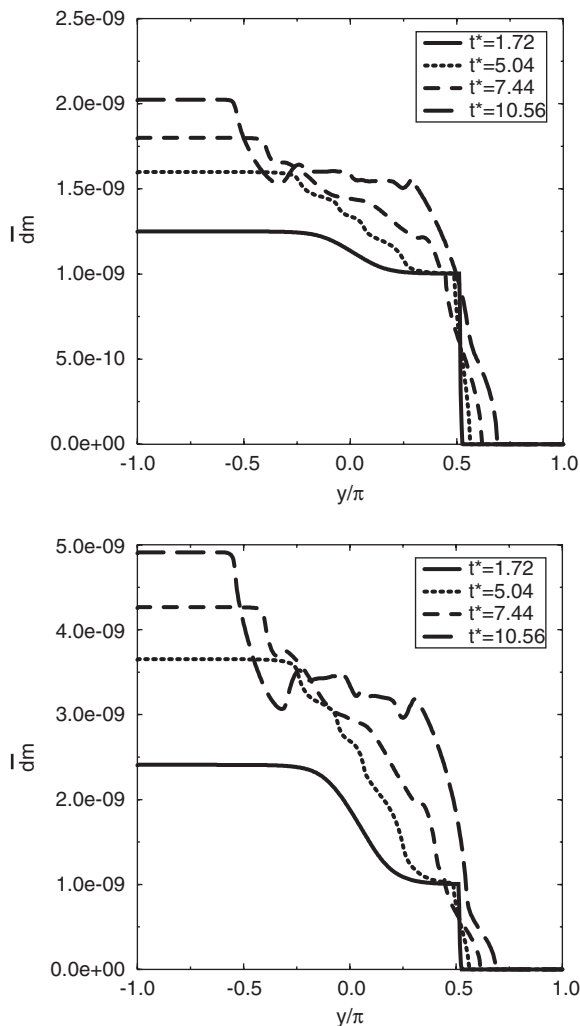


Fig. 10. Cross-stream variation of the mean particle diameter,  $\bar{d}_m$ : (a)  $Da = 1$  and (b)  $Da = 10$ .

is 2.4 nm and at  $t^* = 10.6$  the mean diameter is 4.8 nm. These diameters correspond to increases of 66% and 150% over the values obtained in the  $Da = 1$  flow at the same times, respectively. As a result, the gradient in particle size across the eddy core is higher in the  $Da = 10$  flow. These gradients in size are further magnified during the growth of the eddy.

The GSD is given by

$$[\log(\sigma)]^2 = \frac{\sum_{k=1}^{N_s} Q_k (\log(d_k) - \widehat{\log(d_k)})}{\sum_{k=1}^{N_s} Q_k}, \quad (19)$$

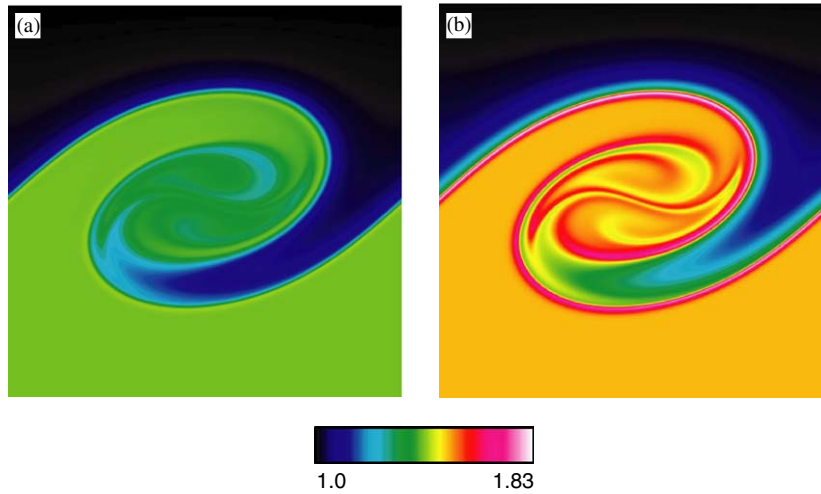


Fig. 11. Instantaneous contours of the geometric standard deviation  $\sigma_g$  at time  $t^* = 10.6$ : (a)  $Da = 1$  and (b)  $Da = 10$ .

where

$$\widehat{\log(d_k)} = \frac{\sum_{k=1}^{N_s} Q_k \log(d_k)}{\sum_{k=1}^{N_s} Q_k}. \quad (20)$$

Instantaneous contours of the GSD for the  $Da = 1$  and  $10$  flows taken at time  $t^* = 10.6$  are shown in Fig. 11. The initial value is unity in the particle-laden stream as all particles are of the same size (1 nm) and zero in the particle-free stream. As the mixing layer evolves and particles of different sizes are created, the geometric standard deviation increases. The images reveal that the GSD is relatively uniform throughout most of the particle-containing fluid. The GSD in the  $Da = 1$  flow is predominantly  $\sigma_g = 1.42$  while in the  $Da = 10$  flow the value is  $\sigma_g = 1.5$ . In both flows the largest values are found along the interface of the particle-free and particle-laden streams. However, in the  $Da = 10$  flow the GSD in this location is  $\sigma_g = 1.83$ . This value is above the self-preserving value for Brownian coagulation using sectional/nodal methods,  $\sigma_g = 1.5$ . Fig. 11(a) suggests that particles in the  $Da = 1$  flow have not yet reached the self-preserving distribution. The value  $\sigma_g = 1.5$  in the  $Da = 10$  flow suggests that the particles have reached the self-preserving distribution for coagulating aerosols away from the eddy. The particle-laden stream contains the largest particles while both the mean diameter and GSD are consistent with a coagulating homogeneous aerosol. However, as one proceeds toward the shear region, the significant differences observed in the GSD arises from the effects of dispersion and transport. The smallest particles are located at the farthest outer edge of the shear interface. These particles are the smallest because the smaller particles preferentially diffuse to the particle-free stream where the lower concentration also decreases the overall coagulation rate, which in turn tends to preserve their size. In fact, the particles in the shear layer have a size distribution considerably smaller than the self-preserving value ( $\sigma_g < 1.5$ ), indicating that the characteristic time for transport is faster than coagulation. As the mixing layer rolls up, we find regions where diffusion effects increase the width of the size distribution over that of the self-preserving limit. The temporal evolution of the GSD is portrayed in the cross-stream profiles shown in Fig. 12. The profiles show that the GSD in the particle-laden stream of the  $Da = 1$  flow is indeed increasing between

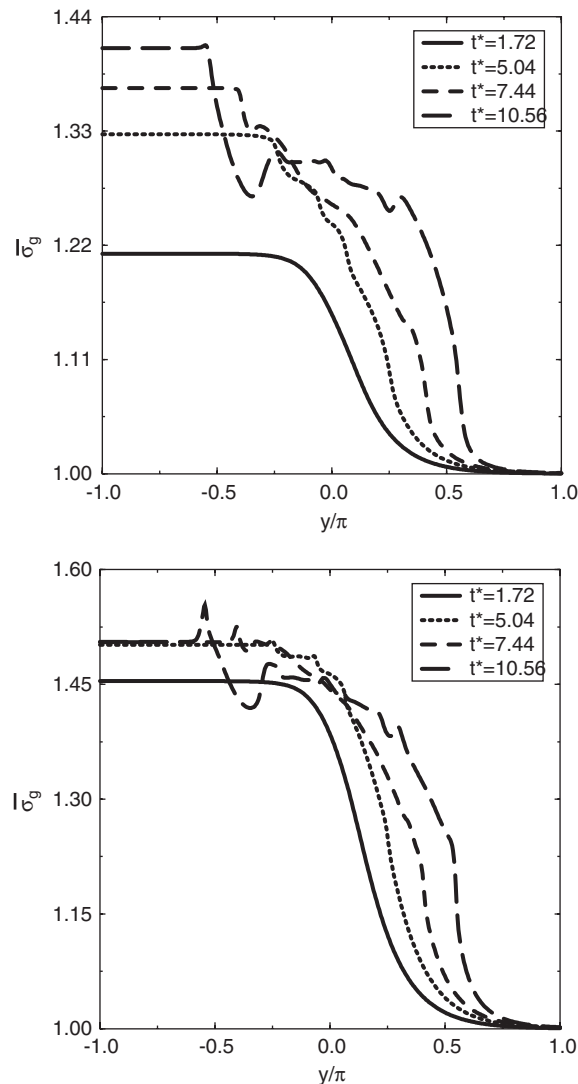


Fig. 12. Cross-stream variation of the geometric standard deviation,  $\overline{\sigma_g}$ : (a)  $Da = 1$  and (b)  $Da = 10$ .

$t^* = 1.72$  and  $10.6$ , while the self-preserving limit is reached in the  $Da = 10$  flow at  $t^* = 5.04$ . There is a decrease in  $\overline{\sigma_g}$  near  $y/\pi = -0.38$  in both flows. These correspond to the aforementioned engulfment of particle-free fluid, which acts to dilute the particle size distribution thereby reducing the GSD. The large  $\overline{\sigma_g}$  values near  $y/\pi = -0.63$  in the  $Da = 10$  flow are due to the transport of small particles away from the particle-laden stream. These trends are consistent with those observed in the study by [Settumba and Garrick \(2003\)](#) which utilized an assumed lognormal distribution and a moment method to predict nanoparticle coagulation in a temporal mixing layer. The moment method is known to work well when coagulation is significant. There is no need to utilize a nodal/sectional method in regimes where a moment method will suffice, especially given the computational cost ([Settumba & Garrick, 2003, 2004](#)). Where

the nodal approach shows its superiority is in its generality and resulting robustness which allows it to capture particle dynamics without many prescriptive constraints.

#### 4. Summary and conclusions

DNS of nanoparticle coagulation in two-dimensional temporal mixing layers was performed. The fluid field was obtained by solving the incompressible Navier–Stokes equations while a nodal representation was employed to approximate the aerosol (GDE). The fluid and particle fields are coupled together and solved in a manner which provides the particle field as a function of space, time and size without the use of turbulence, or other models. The flows simulated consisted of a stream of fluid containing 1 nm diameter particles mixing with a stream of particle-free fluid. A coagulation Damköhler number was defined to represent the ratio of the convective time scale to the coagulation time scale. Simulations were performed for Damköhler numbers of  $Da = 1$  and 10. The simulations were halted when the size of the eddy became too large to be contained within the flow domain. The results revealed that over the time period considered, particles grow faster in the particle-laden stream, away from the effects of large scale mixing and transport. The results also suggest that the growth rate increases with the Damköhler number. The simulations captured the “engulfing” of particle-free fluid and the ensuing local dilution of the particle field. Additionally, the simulations predicted large values of the geometric standard deviation near the interface of the particle-laden and particle-free streams. Instantaneous views of the geometric standard deviation revealed values which were uniform away from particle concentration gradients. From an engineering point of view, this suggests that methods which decrease particle concentration gradients and act to homogenize the particle/flow field may be beneficial in reducing the width of the particle size distribution. However, three-dimensional simulations which capture the vortex bending and stretching present in turbulent flows are needed to fully characterize the flow-field effects on the particle size distribution. The computational expense of the current two-dimensional simulations render DNS almost certainly out of reach. Other methodologies, which can reduce the computational expense, such as large eddy simulation, may offer an avenue to capture the relevant physics of nanoparticle dynamics in turbulent flows. This serves as a basis to assess the performance of subgrid-scale closures in capturing the effects of the unresolved fluid–particle interactions present in turbulent flows containing nanoparticle coagulation.

#### Acknowledgements

The first author acknowledges the support of the National Science Foundation under Grant ACI-9982274. Computational resources are provided by the Minnesota Supercomputing Institute.

#### References

- Bernal, L. P., & Roshko, A. (1986). Streamwise vortex structure in plane mixing layers. *Journal of Fluid Mechanics*, 170, 499–525.
- Brown, G. L., & Roshko, A. (1974). On density effects and large structure in turbulent mixing layers. *Journal of Fluid Mechanics*, 64, 775–816.
- Cain, A. B., Reynolds, W. C., & Ferziger, J. H. (1981). A three-dimensional simulation of transition and early turbulence in a time-developing mixing layer. *Department of Mechanical Engineering Report TF-14*, Stanford University, Stanford, CA.

- Carpenter, M. H. (1990). A high-order compact numerical algorithm for supersonic flows. In: K. W. Morton (Ed.), *12th international conference on numerical methods in fluid dynamics, Lecture notes in physics* (Vol. 371, pp. 254–258). New York, NY: Springer.
- Dagani, R. (2000). Nasa goes nano. *Chemical Engineering News*, 78, 36–38.
- Eaton, J. K., & Fessler, J. R. (1994). Preferential concentration of particles by turbulence. *International Journal of Multiphase Flow*, 20, 169–209.
- Elghobashi, S. E. (1991). Particle-laden turbulent flows: Direct simulation and closure models. *Applied Scientific Research*, 48, 301–314.
- Elghobashi, S. E., & Truesdell, G. C. (1992). Direct simulation of particle dispersion in a decaying isotropic turbulence. *Journal of Fluid Mechanics*, 242, 655–700.
- Frankel, S. H., McMurtry, P. A., & Givi, P. (1995). Linear eddy modeling of reactant conversion and selectivity in homogeneous turbulence. *A.I.Ch.E. Journal*, 41, 258–266.
- Frenklach, M., & Harris, S. J. (1987). Aerosol dynamics modeling using the method of moments. *Journal of Colloid Interface Science*, 118, 252–261.
- Friedlander, K. S. (2000). *Smoke, dust and haze: Fundamentals of aerosol dynamics*. New York, NY: Oxford University Press.
- Friedlander, S. K., & Wu, M. K. (1994). Linear rate law for the decay of the excess surface area of a coalescing solid particle. *Physical Review B*, 49, 3622–3624.
- Fuchs, N. A. (1964). *The mechanics of aerosols*. Oxford, England: Pergamon.
- Gelbard, F., & Seinfeld, J. H. (1980). Simulation of multicomponent aerosol dynamics. *Journal of Colloid and Interface Science*, 78, 485–501.
- Gelbard, F., Tambour, Y., & Seinfeld, J. H. (1980). Sectional representations for simulating aerosol dynamics. *Journal of Colloid and Interface Science*, 76, 541–556.
- Hamaker, H. C. (1937). The London-van der Waals attraction between spherical particles. *Physica*, 4, 1058–1072.
- Jeong, J. I., & Choi, M. (2003). Analysis of non-spherical polydisperse particle growth in a two-dimensional tubular reactor. *Journal of Aerosol Science*, 34, 713–732.
- Kennedy, C. A., & Carpenter, M. H. (1994). Several new numerical methods for compressible shear-layer simulations. *Applied Numerical Mathematics*, 14, 397–433.
- Kennedy, I. M. (1998). Flow field effects on nucleation in a reacting mixing layer. *Physics of Fluids A*, 28, 3515–3524.
- Kerminen, V. M. (1994). Simulation of brownian coagulation in the presence of van der Waals forces and viscous interactions. *Aerosol Science and Technology*, 20, 207–214.
- Kerstein, A. R. (1989). Linear eddy modeling of turbulent transport, II: Application to shear layer mixing. *Combustion and Flame*, 75, 397–413.
- Kerstein, A. R. (1991). Linear-eddy modeling of turbulent transport, Part 6: Microstructure of diffusive scalar mixing fields. *Journal of Fluid Mechanics*, 231, 361–394.
- Kerstein, A. R. (1992). Linear-eddy modeling of turbulent transport, Part 7: Finite-rate chemistry and multi-stream mixing. *Journal of Fluid Mechanics*, 240, 289–313.
- Koch, W., & Friedlander, S. K. (1990). The effect of particle coalescence on the surface area of a coagulating aerosol. *Journal of Colloid and Interface Science*, 140, 419–427.
- Kusters, K. A., Wijers, J. G., & Thoenes, D. (1997). Aggregation kinetics of small particles in agitated vessels. *Chemical Engineering Science*, 52, 107–121.
- Langbein, D. (1974). *Theory of Van der Waals attraction*. New York: Springer.
- Lee, B. W., Oh, S., & Choi, M. (2001). Simulation of growth of nonspherical silica nanoparticles in a premixed flat flame. *Aerosol Science and Technology*, 35, 978–989.
- Lee, K. W., & Chen, H. (1984). Coagulation rate of polydisperse particles. *Aerosol Science and Technology*, 3, 327–334.
- Lehtinen, K. E. J., & Zachariah, M. R. (2001). Self-preserving theory for the volume distribution of particles undergoing brownian coagulation. *Journal of Colloid and Interface Science*, 242, 314–318.
- Lehtinen, K. E. J., & Zachariah, M. R. (2002). Energy accumulation in nanoparticle collision and coalescence processes. *Journal of Aerosol Science*, 33, 357–368.
- Libby, P. A., & Williams, F. A. (Eds.) (1994). *Turbulent reacting flows*. London, UK: Academic Press.
- Lifshitz, E. M. (1956). The theory of molecular attractive forces between solids. *Soviet Physics*, 2, 73–83.
- MacCormack, R. W. (1969). The effect of viscosity in hypervelocity impact catering. *AIAA Paper* 69-354.

- Matsoukas, T., & Friedlander, S. K. (1991). Dynamics of aerosol agglomerate formation. *Journal of Colloid and Interface Science*, *146*, 495–506.
- McGraw, R. (1997). Description of aerosol dynamics by the quadrature method of moments. *Aerosol Science and Technology*, *27*, 255–265.
- McMurtry, P. A., Menon, S., & Kerstein, A. R. (1993). Linear eddy modeling of turbulent combustion. *Energy & Fuels*, *7*, 817–826.
- Metcalfe, R. W., Orszag, S. A., Brachet, M. E., Menon, S., & Riley, J. J. (1987). Secondary instability of a temporally growing mixing layer. *Journal of Fluid Mechanics*, *184*, 207–243.
- Miller, R. S., Madnia, C. K., & Givi, P. (1994). Structure of a turbulent reacting mixing layer. *Combustion Science and Technology*, *99*, 1–36.
- Modem, S., Garrick, S. C., Zachariah, M. R., & Lehtinen, K. E. J. (2002). Direct numerical simulation of nanoparticle coagulation in a temporal mixing layer. In *Proceedings of the 29th symposium (international) on combustion*. The Combustion Institute, Pittsburgh, PA.
- Moser, R. D., & Rogers, M. M. (1993). The three-dimensional evolution of a plane mixing layer: Pairing and transition to turbulence. *Journal of Fluid Mechanics*, *247*, 275–320.
- Pratsinis, S. E. (1998). Flame aerosol synthesis of ceramic powders. *Progress in Energy and Combustion Science*, *24*, 197–219.
- Pratsinis, S. E., & Kim, K.-S. (1989). Particle coagulation, diffusion and thermophoresis in laminar tube flows. *Journal of Aerosol Science*, *20*, 101–111.
- Pyykönen, J., & Jokiniemi, J. (2000). Computational fluid dynamics based sectional aerosol modelling schemes. *Journal of Aerosol Science*, *31*, 531–550.
- Reade, W. C., & Collins, L. R. (2000). A numerical study of the particle size distribution of an aerosol undergoing turbulent coagulation. *Journal of Fluid Mechanics*, *415*, 45–64.
- Reist, P. C. (1993). *Aerosol science and technology* (2nd ed.). New York, NY: McGraw-Hill.
- Riley, J. J., & Metcalfe, R. W. (1980). Direct numerical simulations of a perturbed, turbulent mixing layer. *AIAA Paper 80-0274*.
- Riley, J. J., & Patterson, G. S. (1974). Diffusion experiments with numerically integrated isotropic turbulence. *Physics of Fluids*, *17*, 292–297.
- Roshko, A. (1976). Structure of turbulent shear flows. *AIAA Journal*, *14*, 1349–1357.
- Sandham, N. D., & Reynolds, W. C. (1991). Three-dimensional simulations of large eddies in the compressible mixing layer. *Journal of Fluid Mechanics*, *224*, 133–158.
- Seigneur, C., Hudischewskyj, A. B., Seinfeld, J. H., Whitby, K. T., Whitby, E. R., Brock, J. R., & Barnes, H. M. (1986). Simulation of aerosol dynamics: A comparative review of mathematical models. *Aerosol Science and Technology*, *5*, 205–222.
- Settumba, N., & Garrick, S. C. (2003). Direct numerical simulation of nanoparticle coagulation in a temporal mixing layer via a moment method. *Journal of Aerosol Science*, *34*, 149–167.
- Settumba, N., & Garrick, S. C. (2004). A comparison of diffusive transport in a moment method for nanoparticle coagulation. *Journal of Aerosol Science*, *35*, 93–101.
- Snyder, W. H., & Lumley, J. L. (1971). Some measurements of particle velocity autocorrelation functions in a turbulent flow. *Journal of Fluid Mechanics*, *48*, 41–47.
- Squires, K. D., & Eaton, J. K. (1991). Preferential concentration of particles by turbulence. *Physics of Fluids*, *3*, 1169–1178.
- Sundaram, S., & Collins, L. R. (1997). Collision statistics in an isotropic particle-laden turbulent suspension. Part 1. Direct numerical simulations. *Journal of Fluid Mechanics*, *335*, 75–109.
- Terry, D. A., McGraw, R., & Rangel, R. H. (2001). Method of moments solutions for a laminar flow aerosol reactor model. *Aerosol Science and Technology*, *34*, 353–362.
- Vemury, S., & Pratsinis, S. E. (1995a). Corona-assisted flame synthesis of ultrafine titania particles. *Applied Physics Letters*, *66*, 3275–3277.
- Vemury, S., & Pratsinis, S. E. (1995b). Self-preserving size distributions of agglomerates. *Journal of Aerosol Science*, *26*, 175–185.
- Vemury, S., Pratsinis, S. E., & Kibbey, L. (1997). Electrically controlled flame synthesis of nanophase TiO<sub>2</sub>, SiO<sub>2</sub> and SnO<sub>2</sub> powders. *Journal of Material Research*, *12*, 1031–1042.
- Williams, F. A. (1985). *Combustion theory* (2nd ed.). Menlo Park, CA: The Benjamin/Cummings Publishing Company.
- Williams, F. A. (1989). Structure of flamelets in turbulent reacting flows and influences of combustion on turbulence fields. In R. Borghi & S. N. B. Murthy (Eds.), *Turbulent reactive flows, Lecture notes in engineering* (Vol. 40, pp. 195–212). New York, NY: Springer.

- Wooldridge, M. S. (1998). Gas-phase combustion synthesis of particles. *Progress in Energy and Combustion Science*, 24, 63–87.
- Wright, D. L., McGraw, R., & Rosner, D. E. (2001). Bivariate extension of the quadrature method of moments for modeling simultaneous coagulation and sintering of particle populations. *Journal of Colloid and Interface Science*, 236, 242–251.
- Wright, D. L., Yu, S., Kasibhatla, P. S., McGraw, R., Schwartz, S. E., Saxena, V. K., & Yue, G. K. (2002). Retrieval of aerosol properties from moments of the particle size distribution for kernels involving the step function: Cloud droplet activation. *Journal of Aerosol Science*, 33, 319–337.
- Wu, J., & Menon, S. (2001). Aerosol dynamics in the near field of engine exhaust plumes. *Journal of Applied Meteorology*, 40, 795–809.
- Xiong, Y., Akhtar, M. K., & Pratsinis, S. E. (1993). Formation of agglomerate particles by coagulation and sintering—part II: The revolution of the morphology of aerosol made titania, silica and silica-doped titania powders. *Journal of Aerosol Science*, 24, 301–313.
- Xiong, Y., & Pratsinis, S. E. (1993). Formation of agglomerate particles by coagulation and sintering—part I: A two-dimensional solution of the population balance equation. *Journal of Aerosol Science*, 24, 283–300.
- Zachariah, M. R., & Semerjian, H. G. (1989). Simulation of ceramic particle formation: Comparison with in-situ measurements. *A.I.Ch.E. Journal*, 35, 2003–2012.
- Zhang, Y., Seigneur, C., Seinfeld, J. H., Jacobson, M. Z., & Binkowski, F. S. (1999). Simulation of aerosol dynamics: A comparative review of algorithms used in air quality models. *Aerosol Science and Technology*, 31, 487–514.
- Zhu, W., & Pratsinis, S. (1996). Flame synthesis of nanosize particles: Effect of flame configuration and oxidant composition. In: G.-M. Chow, K.E. Gonsalves (Eds.), *Nanotechnology: ACS Symposium Series* (Vol. 622, pp. 64–78). Oxford: Oxford University Press.